A Simple Method for Extracting Symmetry from Meshes

Simge Tekin and Yusuf Sahillioğlu

***Abstract*—Motivated by the importance and universality of symmetry detection problem, we present a simple yet effective solution that is able to identify symmetric correspondences as well as the symmetry axis curve on a given mesh model embedded in 3D. We consider global intrinsic reflective symmetry that is invariant to isometric, i.e., distance-preserving, pose changes of the input model. The key insight to our solution is to minimize the deviation from isometry in the constructed symmetric self-maps by generating base vertices and feature vectors in coarse-to-fine manner. Comparison with the state-of-the-art methods reveals the timing and simplicity advantages of the proposed method, whereas our accuracy is almost tied with them. Our method does not require any initialization and does not demand restrictions on topology, tessellation, and resolution.**

I. Introduction

Symmetry does not only serve aesthetic considerations, e.g., beauty of human faces, but also physical and algorithmic optimality principles. We can exemplify the physical aspect with architectural constructions and the latter with geometry processing algorithms such as automatic discovery of surface maps [8].

We address the important problem of symmetry detection in geometry processing. Namely, we detect reflectively symmetric correspondences as well as the reflective symmetry axis on digital models embedded in 3D space. Our output correspondences and axis are invariant to the isometric, i.e., distance-preserving, pose changes of the query model. We, consequently, consider reflective intrinsic symmetry. Compared to the well-studied and easier extrinsic counterpart, e.g., symmetry of Eiffel Tower, extraction of intrinsic symmetry information requires a huge search space involving rotations, translations and bends, e.g., human motions. We consequently cast an optimization problem that can efficiently and effectively analyze this space.

Key insight to our symmetric map computation is the preservation of pairwise geodesic distances to the carefully selected and matched base vertices. Symmetry axis extraction is performed afterwards via voting once the symmetric matches and side information of the vertices are made available. Our method is resilient to small deviations from isometry that are due to imperfections of the modeling process and/or geometry discretization errors. It handles the extrinsic symmetry naturally, yet replacing intrinsic geodesic distances with Euclidean distances will lead to a faster extrinsic method in this simpler scenario. Our method, however, does not handle rotational symmetries and does not support symmetry extraction on partial shapes where some of the symmetric regions are missing, e.g., human with no left leg.

S. Tekin and Y. Sahillioğlu are with the Department of Computer Engineering, Middle East Technical University, Turkey (ys@ceng.metu.edu.tr).

II. Related Work

For the reflectional symmetry, which is the focus of our paper, papers work on extrinsic and intrinsic levels where the former and latter consider the Euclidean and geodesic distance compatibilities, respectively [10]. Our algorithm operates on intrinsic level, hence the focus of this literature review.

Most of the objects around us do not lose their reflective symmetry even if they are isometrically bent, e.g., eyeglasses in and out of pocket, humans sitting and standing, etc. Despite being this common, the first study dealing with the symmetry of bendable/articulated isometric objects is seen only recently in 2007 [13]. It adapts generalized multidimensional scaling, a method that embeds one surface onto the other for surface pair matching, in order to detect global reflective intrinsic symmetries. Similarly, [7] converts a matching method that works on surface pairs into their method that maps surface to itself. Specifically, it votes through the Möbius transformations defined over genus zero surfaces. The probabilistic framework in [20] detects intrinsic symmetry by estimating the likelihood two point pairs belong to symmetries at the same scale. From a small number of symmetric pairs of points, [19] determines intrinsic symmetries that are represented as linear transformations of functional space on shapes.

Symmetry computation under mild noise is also explored. To this end, [12], [11] use the heat diffusion properties via the eigenfuctions of the Laplace-Beltrami operator in order to produce self-maps, i.e., mapping the right side of the surface to its own left. Same spectrum is employed later in [14] in an effort to extend [13] into a more stable method under a certain amount of topological noise. Alternatively, skeletons can be used for intrinsic symmetry detection in order to alleviate the problems due to the distorted geodesics under such noise [6].

A different branch of methods explicitly change the spatial coordinates of the input model in order to make it look more symmetric [9], [16]. Direct Euclidean distances or other extrinsic tactics such as smooth shape diameter signature [5] and fully-convolutional symmetry prediction network [18] can then be utilized on these new forms.

III. Method

Given a source and target model, our method operates in three steps. At first, we extract symmetric correspondences of the extreme points and divide the model into five regions. In the second step, based on the symmetric correspondences, we map the points in source regions to their intrinsically symmetric target region correspondences. We finally extract the symmetry axis curve based on these mappings. Note that although our method can be applied to any model with bilateral symmetry (Section V), we use human hand and human foot metaphors in order to make the reading in the sequel easier.

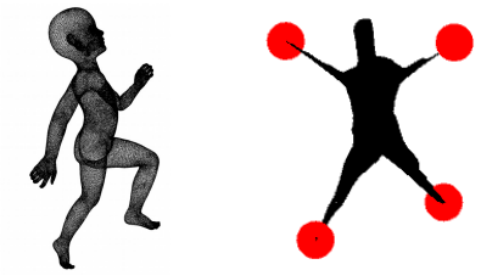

Fig. 1: Kid model at left and its 3D spectral embedding with highlighted extreme points (red).

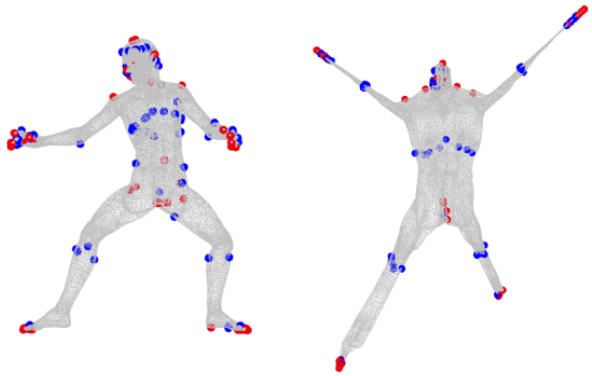

Fig. 2: Sets S_1 (red) and S_2 (blue) on David model in spatial domain (left) and after spectral embedding (right).

A. Extreme Points Mapping

We find correspondences of extreme points, namely, tip of hands and feet. Upcoming denser maps will be based on these extreme points matches. We observe that the embeddings of models in spectral domain concretizes the limbs, making the extreme points farther from each other. We embed the meshes in spectral domain as defined in [3]. To this end, we construct the affinity matrix by using evenly-spaced hundred landmark vertices [4], and obtain embeddings of them at first via classical multidimesional scaling as described in [17]. Then we embed the remaining vertices on the mesh by scaling the geodesic distances to these landmarks. In this way, we did not need to compute the geodesics for all vertices, saving both computation and storage.

Afterwards, we sample four vertices that are geodesically farthest from each other [4]. These vertices would correspond to the tip of hands and feet, forming the extreme points set $E = \{h_1, h_2, f_1, f_2\}$.

In order to detect hand-to-hand and foot-to-foot correspondences, we follow a number of steps, some of them having side effects that will be useful later. Firstly, we approximate the average geodesic distance function (AGD) [7] by approximating geodesic distances on surface using Dijkstra's algorithm, and smoothing AGD over 1-ring neighborhoods. To speed up the computation of AGD, we use hundred vertices on the embedded mesh model that are again determined by farthest point sampling algorithm [4]. Note that we did not use the hundred sample vertices that we used to construct affinity matrix since the geodesics computed for them was for the mesh in spatial domain. Our experiments suggest that geodesics on spectrally embedded mesh yield better AGD values for the upcoming S_1 and S_2 construction. We form the set S_1 with the local extrema (namely maxima) of AGD values over 1-rings. For the purpose of computing minimal geodesic distance (MGD) that is assigned to every vertex of the mesh, we use S_1 as described in [7]. Namely, MGD for a given vertex is the geodesic distance to the closest vertex in the set S_1. Similarly, local maxima of the MGD values form the set S_2. Figure 2 shows S_1 and S_2 on a model. These sets will be used later in Section III-C.

We then sort the four extreme vertices with respect to their MGD values and group the two with the smallest MGDs and the other two with the largest MGDs. The vertices in these groups are naturally the symmetric correspondences of each other. For low-resolution models with less stable Dijkstra-based geodesics, performing this operation with AGD values instead of MGD values is more successful while extracting hand-to-hand and foot-to-foot correspondence. The main reason is the smoothness of AGD which is defined by integrating geodesic distances. MGD, on the other hand, is defined using single geodesic distances and therefore it tends to be irregular and unstable. Thus, we use AGD while matching extreme vertices on low-resolution meshes, e.g., less than 30K vertices, and MGD for the high-resolution models.

B. Initial Region Assignments

Next step is to detect the two extreme vertices that are on the same side of the symmetry axis curve, e.g., left hand and left foot. In order to achieve this, we use geodesic distances between the extreme vertices that are not symmetric correspondences of each other, i.e., one extreme vertex from one group, e.g., $\{h_1, h_2\}$, and the other extreme from the other group, e.g., $\{f_1, f_2\}$. If $d_g(h_1, f_1) < d_g(h_1, f_2)$, then h_1 and f_1 are assumed to be on same side of the symmetry axis curve as they would be in a standard human body. After this step, we revert the model back to spatial domain, by changing spectral coordinates of vertices with the values they have in the original form.

Using midpoints of the extreme vertex correspondences, at first we define two source regions and two target regions on mesh model M:

$$R_{\text{source1}} = \{v \in M | d_g(v, h_1) < d_g(v, m_{h_1,h_2})\} \quad (1)$$

$$R_{\text{target1}} = \{v \in M | d_g(v, h_2) < d_g(v, m_{h_1,h_2})\} \quad (2)$$

$$R_{\text{source2}} = \{v \in M | d_g(v, f_1) < d_g(v, m_{f_1,f_2})\} \quad (3)$$

$$R_{\text{target2}} = \{v \in M | d_g(v, f_2) < d_g(v, m_{f_1,f_2})\} \quad (4)$$

where m_{h_1,h_2} is the midpoint of the extreme match $h_1 \leftrightarrow h_2$ and m_{f_1,f_2} is defined similarly. Now, we have two source-target region pairs that are symmetrically equivalent, e.g., left

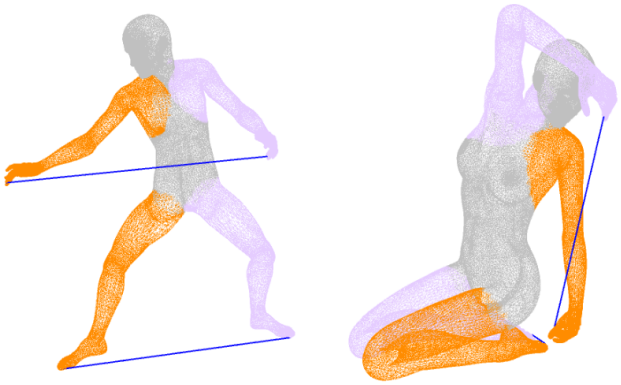

Fig. 3: Source regions (orange), target regions (purple), and the fifth region (gray) along with the mapping of extreme vertices. Regions including an extreme vertex and its correspondence has source-target relationships.

arm with shoulder and right arm with shoulder. We also know that two sources are on the same side with respect to the symmetry axis curve while two target regions are on the other side. The remaining vertices that are not in these four regions form a fifth region that works as both source and target, hence no sixth region is required. As a result of this process, we obtain four regions for which we know pairwise symmetrical source and target relationship and one region without that information (see Figure 3). Purpose of extracting these regions is to narrow down the search space to a target region instead of whole mesh while processing a vertex in source region.

C. Dense Symmetric Mapping and Symmetry Axis Curve

The key observation that drives our dense symmetric mapping computation and symmetry axis computation is the following. If some vertex $p \in M$ and $q \in M$ are symmetrical correspondences of each other, and some $s \in M$ is determined to be on symmetry axis curve, i.e., midpoint of the path connecting p and q, then $d_{\mathrm{g}}(p,s)$ and $d_{\mathrm{g}}(q,s)$ should be equal independent of the pose. Also, if p' and q' are symmetrical correspondences, $d_{\mathrm{g}}(p,p')$ and $d_{\mathrm{g}}(q,q')$ are expected to be equal. In practice, however, since bends caused by pose can distort shortest paths, $d_{\mathrm{g}}(p,s)$ and $d_{\mathrm{g}}(q,s)$ might not be equal. Our goal is therefore to use geodesic distances as a similarity measure in correspondence extraction while *minimizing* this distortion by using a group of base vertices. Consequently, the procedure is based on feature vectors that are made up of geodesic distances to some predetermined base vertices. We implement an iterative procedure where previously extracted correspondences enhance the upcoming extractions by introducing new base vertices. We proceed in 4 stages.

Stage 1: For the first stage of the dense map computation, the base vertices are determined to be i) extreme vertices, ii) m_h: midpoint of h_1-h_2 path, iii) m_f: midpoint of f_1-f_2 path, and iv) m_{hf}: midpoint of the path between the midpoints of h_1-f_1 and h_2-f_2 paths. Midpoints are shown in the inset where blue is the m_{hf}. Although the base point set is defined as $B = \{h_1, h_2, f_1, f_2, m_h, m_f, m_{hf}\}$, for feature vector construction of a vertex, we use extreme vertices that are detected to be on the same side as the vertex (midpoints are always used regardless of the side). For example, if h_1, f_1 and source regions are on the same side, then for a vertex in one of the source regions, base vertices that are used to construct the feature vector are $\{h_1, f_1, m_h, m_f, m_{hf}\}$. Similarly, for a vertex in one of the target regions, these vertices would be $\{h_2, f_2, m_h, m_f, m_{hf}\}$.

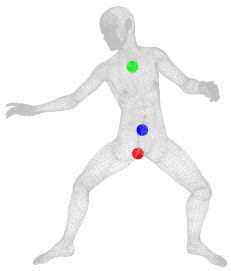

In the first stage, we perform the mapping on S_1 that we formed before (Section III-A). Reason for this is that S_1 is a symmetry invariant vertex set, and includes much smaller number of elements compared to the whole mesh. This gives us a small area to search for robust mappings. We divide the vertices in S_1 into source and target regions according to the region they fall into. We ignore the vertices on S_1 that are on the fifth region on this stage. Thus, only the vertices that are on both S_1 and one of the arm and leg regions presented on Figure 3 are matched.

Feature Vector Creation: The fundamental component that is required for mapping at any stage is the feature vector, which we attach to all vertices. For a vertex, v, on the same side as h_1 and f_1, e.g., source region, the feature vector is created initially as a 5 dimensional vector ρ:

$$\rho = (d_{\mathrm{g}}(v,h_1), d_{\mathrm{g}}(v,f_1), d_{\mathrm{g}}(v,m_h), d_{\mathrm{g}}(v,m_f), d_{\mathrm{g}}(v,m_{hf})) \tag{5}$$

Feature vector for a vertex v' in the corresponding target region of that source region is then the following:

$$\rho' = (d_{\mathrm{g}}(v',h_2), d_{\mathrm{g}}(v',f_2), d_{\mathrm{g}}(v',m_h), d_{\mathrm{g}}(v',m_f), d_{\mathrm{g}}(v',m_{hf})) \tag{6}$$

To map vertices from source region to target region, we choose the vertex v' in the target region that minimizes D:

$$D = \sum_{i=1}^{5} \left(\frac{\rho_i - \rho_i'}{\rho_i}\right)^2 \tag{7}$$

We use these feature vectors to map vertices in S_1 that fall into two source and two target regions. At the end of mapping procedure for a region, we extract midpoints of at most five correspondences with the smallest D values, i.e., if there are more than five matches between two regions, we pick the best five. Distances to these midpoints are appended as new dimensions to the growing feature vector of the vertex v. We also append the distances to the endpoints of the S_1-based correspondences that are on the same side as v. Similar appends take place for v' as well.

Stage 2: For the second stage, we match the set S_2 obtained in (Section III-A). Similar to what we do in the mapping of S_1, we divide S_2 into two source and two target regions depending on their positions. We then compute the mapping while adding new dimensions to feature vector similar to Stage 1, e.g., we append distances to the midpoints from all region-to-region mappings as well as distances to the endpoints at the correct side.

Stage 3: Thus far, each match provides two dimensions to the feature vector, namely distance to its midpoint and to the endpoint of correct side. In this stage, we remove the dimensions due to the endpoints and keep only the midpoint-based dimensions. The reason is that, the endpoints can only be selected from the restricted $S1$ and $S2$ sets and hence are prone to errors; errors are tolerable since $S1$ and $S2$ are symmetry-invariant vertices but still we observe that they are not as stable as the midpoints they provide. For example, a match running from source shoulder to target armpit has slightly incompatible endpoints but a stable midpoint that is on the ideal symmetry axis, which makes it useful as a feature vector base vertex.

For this stage, we sparsely sample hundred [4] vertices on two source regions and the fifth center region (Fig. 3). This stage aims to find correspondences of to these samples. For all sample vertices in the source regions, we again seek the match in their corresponding target regions, where all region vertices are considered as match candidates. For all sample vertices in the fifth region, we consider each vertex from the same region as a match candidate.

We then take the best 20 best matches (minimizing D) from each region-to-region mappings and use their midpoints to grow the feature vectors further. For the feature vector of the vertex v, we also append the distances to the endpoints of these correspondences that are on the same side v.

Stage 4: We perform the mapping between all hundred samples in this stage but using the latest feature vectors that include the distances to both the endpoints and midpoints of the matches obtained in Stage 3. Note that we include the endpoints as well since they are more reliable and evenly distributed than the restricted sets $S1$ and $S2$ that we discard after Stage 2. We keep the best 30 matches (minimizing D) from each region-to-region mappings.

For all correspondences, we evaluate the side of the vertices that form the correspondence as described in the sequel. If side of both vertices in a given correspondence is the same, we eliminate that correspondence. Finally, in order to detect the vertices that are on the symmetry axis region, we decide the side of each vertex as either source or target. We then add the vertex to the symmetry axis curve if its 1-ring neighborhood consists of a hybrid set of source and target side labels.

Side Decision: We note that our algorithm is not sensitive to the potential mistakes in the initial region assignments of Section III-B. These mistakes rarely arise due to discretization errors when left hand happens to be closer to the right foot instead of the left foot; in this case the left hand region, i.e. the left arm with shoulders (Figure 3), and the right foot region, i.e., the right leg, are labeled as source regions although they are at different sides of the symmetry axis in reality. This is definitely not a problem during the symmetric correspondence computations because foot region is mapped to the other foot region regardless of what their labels are, i.e., source or target. This is, however, a problem during symmetry axis extraction which depends on the side labels of each mesh vertex. As a solution to this problem, we reevaluate the side label of the newly matched vertex and possibly change it from source to target or vice versa. The change is made for vertex v depending on its distances to the previously matched vertices whose sides are known. Specifically, we count the number of endpoints in the previous matches that are closer to v than their symmetric endpoints. We accept v to be on the side for which the count is higher. Thus, a vertex that is determined to be on left side can be determined to be on right side later.

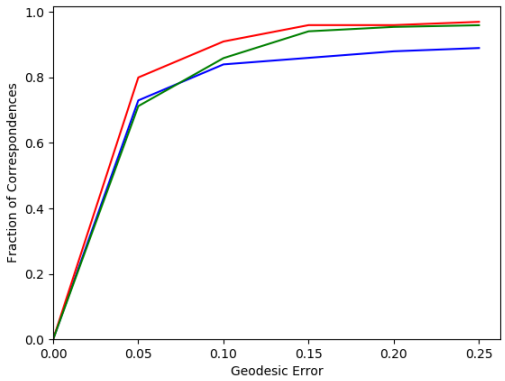

Fig. 4: Geodesic Error plots of our results on KIDS (blue), SCAPE (green), and TOSCA (red) datasets.

IV. Results

We conducted experiments on three different datasets: SCAPE [1], TOSCA [2], and KIDS [15] in order to obtain quantitative and qualitative results of the extracted symmetry information by our algorithm. Symmetry information consists of the symmetric correspondences and the symmetry axis.

SCAPE, a reconstructed pose sequence of a human actor contains 71 non-uniformly sampled 12K-vertex models with the fixed template connectivity. We use the high-resolution Cat, David, Gorilla, Michael, Victoria, and Wolf objects from TOSCA, each class representing the motion of an articulated object with 11, 7, 4, 18, 12, and 3 meshes, respectively, where humans have about 50K vertices and the others about 25K. KIDS dataset, consisting of 32 meshes of two kid models, has fixed connectivity over 60K vertices. Ground-truth information for a subset of $\sim$20 symmetric vertices are given for SCAPE and TOSCA by [7], whereas this information is given for all the vertices of KIDS models. Ground-truth subset corresponds to the informative parts, e.g., ears and eyes.

We employ the Correspondence Rate and Mesh Rate evaluation metrics that are used by Möbius Transformations (MT) [7] and Fast and Accurate Intrinsic Symmetry Detection (FAISD) [11] methods in order to provide fair comparisons. We also introduce Geodesic Error in order to gain additional insight about the accuracy of our results.

1. Geodesic Error: The fraction of correspondences that has geodesic distance between $m(v)$ and $g(v)$ less than a given amount where the maximum distance over the surface is normalized to 1. Here, $m(v)$ is the automatically computed match of v whereas $g(v)$ is the ground-truth match.

Dataset	Corr. Rate	Mesh Rate
SCAPE	81%	75%
TOSCA	87%	88%
KIDS	84%	88%

TABLE I: Performance of our algorithm on SCAPE, TOSCA and KIDS datasets.

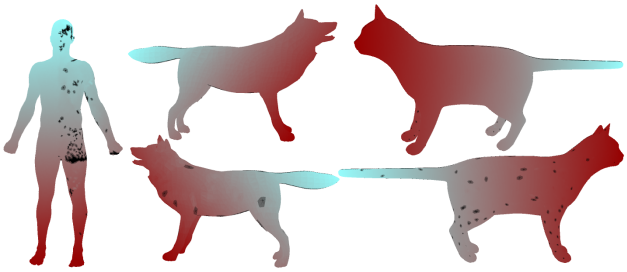

Fig. 5: Transfer of colors on one side to the other using our dense symmetric maps on SCAPE human and TOSCA animals. Unmatched vertices are shown in black.

2. Correspondence Rate: The percentage of correspondences with geodesic distance between the computed and ground-truth correspondence of the vertex less than $\sqrt{\frac{area(M)}{\pi N}}$. We take $N = 20$ as used in MT.

3. Mesh Rate: The percentage of meshes for which the correspondence rate above is more than 75%, as used in MT.

Table I shows Correspondence Rate and Mesh Rate whereas Figure 4 depicts the average Geodesic Error of KIDS, SCAPE and TOSCA datasets. We can observe the fraction of mappings that has smaller geodesic error than 0.05, 0.1, 0.15, 0.2 and 0.25 while maximum possible error is 1. The plot and rates of KIDS dataset represent the evaluation of all correspondences extracted on Stage 4 of our algorithm ($\sim$150 matches), while SCAPE and TOSCA counterparts represent the evaluation of correspondences for provided subset of vertices with ground-truth data ($\sim$20 matches). We use our Stage 4 mapping to define the base vertices and feature vectors that match any other vertex in dense correspondence mode (Figure 5). Similarly, based on our Stage 4 mapping we match the specific $\sim$20 vertices which have ground-truth correspondences as designated by the MT method.

Figure 6 displays symmetry axis curves obtained by our algorithm. We observe accurate curves under large isometric deformations thanks to our robust dense vertex side labeling procedure that is based on the $\sim$150 matches coming from our Stage 4. In addition to the symmetry axis curves, Figure 7 and Figure 8 demonstrate our matches for which ground-truth data is available (MT). Since the ground-truth data is available for all vertices in KIDS, we display all of our Stage 4 matches along with the extracted symmetry curve in Figure 9.

In our experiments, we observe that, especially for low resolution meshes, the Correspondence Rate for failed models is very low while for successful models this rate is high. Thus, failed models significantly decrease the average Correspon-

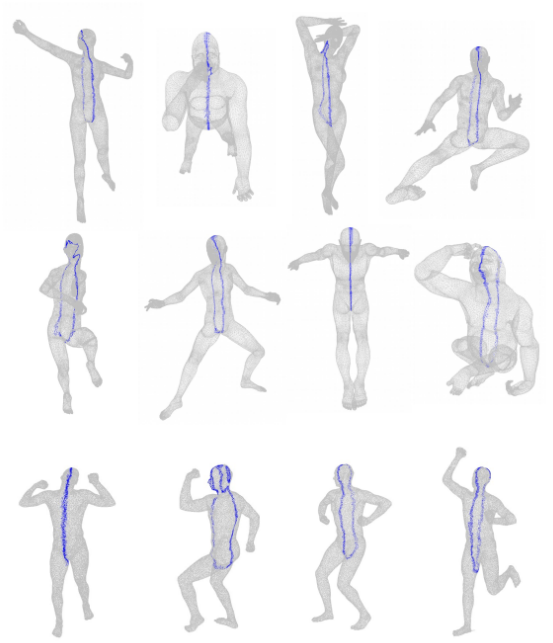

Fig. 6: Global intrinsic reflective symmetry axis curves extracted by our algorithm on TOSCA (first two rows) and SCAPE (last row) models.

Fig. 7: Extracted symmetry axis curves on TOSCA (first two rows) and SCAPE (last row) models along with a subset of our matches for which ground-truth correspondence is known.

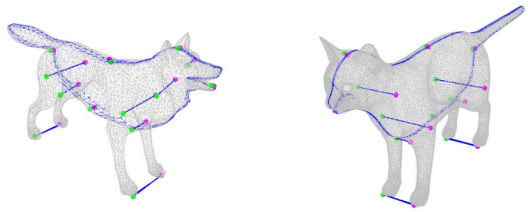

Fig. 8: Our result set consisting of symmetry axis curve and symmetric correspondences on TOSCA Wolf and Cat models. Symmetric correspondences are restricted to vertices whose ground-truth matches are known.

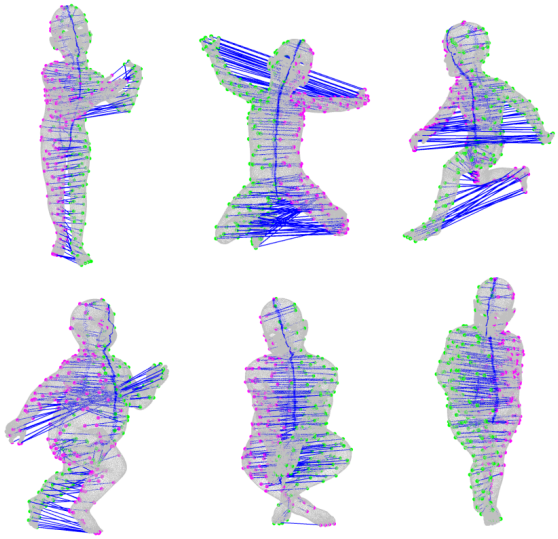

Fig. 9: Our Stage 4 mapping along with the symmetry axis curve for thin kid (first row) and fat kid (second row) models from the KIDS dataset.

dence Rate of a dataset (Tables I-II). We compare the results of our method with MT [7] and FAISD [11] on SCAPE and TOSCA only as they have not used KIDS dataset in their test suites (Table II). We avoid the eigenfunction sign flip and order switch problems of FAISD. We also avoid the costly space search of MT through all possible sample vertex triplets that define Möbius transformations for genus zero surfaces. Our algorithm can work with any genus.

On a 2.3GHz i5 laptop, it takes 7 seconds to obtain our Stage 4 map and then 23 more seconds to compute the full map over 12K vertices of a SCAPE model. The corresponding numbers for a 4K TOSCA Wolf are 2 seconds and 1 sec, whereas 27K Cat requires 27 and 105 seconds. This nearly-quadratic growth in time makes our algorithm practical to map high resolution models to themselves. Note that symmetry axis computation happens instantly as we traverse all vertices in linear time while checking the hybrid labeling situation in their 1-ring neighborhood. Completing Stage 4 is sufficient in order to perform this axis computation operation, e.g., 7 seconds for the symmetry axis curve of a SCAPE model.

	MT	FAISD	Ours	MT	FAISD	Ours
Victoria	83%	96%	78%	63%	100%	75%
Gorilla	-	100%	98%	-	100%	100%
David	82%	96%	95%	57%	100%	100%
Wolf	100%	100%	97%	100%	100%	100%
Cat	66%	96%	65 %	54%	100%	64%
Michael	87%	97%	88%	75%	100%	90%
SCAPE	82%	97%	81%	72%	98%	75%

TABLE II: Correspondence rates (first 3 column from the left) and mesh rates (last 3 columns from the left) for SCAPE and human-shaped classes of TOSCA for MT, FAISD, and our proposed method.

V. Limitations

Although our method is sufficiently generic handling popular human and four-legged animals, it will fail if the input model does not posses bilateral symmetry with four extreme points, e.g., octopus model. Although we did not encounter a case in practice where the extreme points are wrongly detected by taking the first 4 samples of the farthest point sampling procedure [4], i.e, tip of hands and feet is not selected, it is theoretically possible to start with the wrong sample set, an error that cannot be recovered later by the upcoming stages. We finally note our global symmetry method will fail under partial symmetry cases where self-similarities occur only on parts of a shape.

VI. Conclusion and Future Work

We presented a fast and robust algorithm for the global reflective intrinsic symmetry problem. By proper selection of base vertices and the corresponding feature vectors in coarse-to-fine manner, we were able to produce promising symmetric maps at sparse and dense levels. As a by-product, we instantly computed the symmetry axis curve that is invariant to isometric deformations. Our method requires no initial landmark matches, is insensitive to surface triangulation, and can be applied to shapes with arbitrary genus and resolution. Our performance is on a par with the more advanced and slower state-of-the-art methods we compared with.

One future work direction is to enhance the region selection mechanism in order to consider partial and rotational symmetries. While constructing k-nearest neighbor graph is mostly sufficient for the extraction of geodesic distances on point clouds, one can investigate alternative and more robust solutions to extract symmetry on this input type. Another future work can address data compression issue since symmetry can be interpreted as information redundancy. Finally, detection of symmetric partner points can help in the design of a symmetry-aware sampling algorithm that can be useful for various geometry processing tasks such as pairwise shape correspondence.

ACKNOWLEDGEMENTS

This work was supported by TUBITAK (The Scientific and Technological Research Council of Turkey) under the project EEEAG-119E572. We share the source code and the executables of our method as well as the output files at http://www.ceng.metu.edu.tr/∼ys/pubs/sym.zip.

REFERENCES

[1] Dragomir Anguelov, Praveen Srinivasan, Daphne Koller, Sebastian Thrun, Jim Rodgers, and James Davis. Scape: shape completion and animation of people. In *ACM SIGGRAPH 2005 Papers*, pages 408–416. 2005.

[2] Alexander M Bronstein, Michael M Bronstein, and Ron Kimmel. *Numerical geometry of non-rigid shapes*. Springer Science & Business Media, 2008.

[3] Vin De Silva and Joshua B Tenenbaum. Global versus local methods in nonlinear dimensionality reduction. In *NIPS*, volume 15, pages 705–712, 2002.

[4] Yuval Eldar, Michael Lindenbaum, Moshe Porat, and Yehoshua Y Zeevi. The farthest point strategy for progressive image sampling. *IEEE Transactions on Image Processing*, 6(9):1305–1315, 1997.

[5] Josef Graus, Alec Jacobson, and Yotam Gingold. Interacting with self-similarity. *Computer-Aided Design*, 130:102931, 2021.

[6] Wei Jiang, Kai Xu, Zhiquan Cheng, and Hao Zhang. Skeleton-based intrinsic symmetry detection on point clouds. *Graphical Models*, 75(4):177–188, 2013.

[7] Vladimir G Kim, Yaron Lipman, Xiaobai Chen, and Thomas Funkhouser. Möbius transformations for global intrinsic symmetry analysis. In *Computer Graphics Forum*, volume 29, pages 1689–1700. Wiley Online Library, 2010.

[8] Tianqiang Liu, Vladimir G Kim, and Thomas Funkhouser. Finding surface correspondences using symmetry axis curves. In *Computer Graphics Forum*, volume 31, pages 1607–1616. Wiley Online Library, 2012.

[9] Niloy J Mitra, Leonidas J Guibas, and Mark Pauly. Symmetrization. *ACM Transactions on Graphics (TOG)*, 26(3):63–es, 2007.

[10] Niloy J Mitra, Mark Pauly, Michael Wand, and Duygu Ceylan. Symmetry in 3d geometry: Extraction and applications. In *Computer Graphics Forum*, volume 32, pages 1–23. Wiley Online Library, 2013.

[11] Rajendra Nagar and Shanmuganathan Raman. Fast and accurate intrinsic symmetry detection. In *Proceedings of the European Conference on Computer Vision (ECCV)*, pages 417–434, 2018.

[12] Maks Ovsjanikov, Jian Sun, and Leonidas Guibas. Global intrinsic symmetries of shapes. In *Computer graphics forum*, volume 27, pages 1341–1348. Wiley Online Library, 2008.

[13] Dan Raviv, Alexander M Bronstein, Michael M Bronstein, and Ron Kimmel. Symmetries of non-rigid shapes. In *2007 IEEE 11th International Conference on Computer Vision*, pages 1–7. IEEE, 2007.

[14] Dan Raviv, Alexander M Bronstein, Michael M Bronstein, Ron Kimmel, and Guillermo Sapiro. Diffusion symmetries of non-rigid shapes. In *Proc. 3DPVT*, volume 2. Citeseer, 2010.

[15] Emanuele Rodola, Samuel Rota Bulo, Thomas Windheuser, Matthias Vestner, and Daniel Cremers. Dense non-rigid shape correspondence using random forests. In *Proceedings of the IEEE Conference on Computer Vision and Pattern Recognition*, pages 4177–4184, 2014.

[16] Yusuf Sahillioğlu and Ladislav Kavan. Detail-preserving mesh unfolding for nonrigid shape retrieval. *ACM Transactions on Graphics (TOG)*, 35(3):1–11, 2016.

[17] Yusuf Sahillioğlu and Yücel Yemez. Minimum-distortion isometric shape correspondence using em algorithm. *IEEE transactions on pattern analysis and machine intelligence*, 34(11):2203–2215, 2012.

[18] Yifei Shi, Junwen Huang, Hongjia Zhang, Xin Xu, Szymon Rusinkiewicz, and Kai Xu. Symmetrynet: learning to predict reflectional and rotational symmetries of 3d shapes from single-view rgb-d images. *ACM Transactions on Graphics (TOG)*, 39(6):1–14, 2020.

[19] Hui Wang and Hui Huang. Group representation of global intrinsic symmetries. In *Computer Graphics Forum*, volume 36, pages 51–61. Wiley Online Library, 2017.

[20] Kai Xu, Hao Zhang, Wei Jiang, Ramsay Dyer, Zhiquan Cheng, Ligang Liu, and Baoquan Chen. Multi-scale partial intrinsic symmetry detection. *ACM Transactions on Graphics (Special Issue of SIGGRAPH Asia)*, 31(6):181:1–181:10, 2012.

Simge Tekin is a senior undergraduate student in the Department of Computer Engineering at Middle East Technical University, Turkey. She is also a scholar in the Intern Researcher program of TUBITAK, The Scientific and Technological Research Council of Turkey.

Yusuf Sahillioğlu is an associate professor in the Department of Computer Engineering at Middle East Technical University. He is also an associate editor of The Visual Computer journal. His research interests include digital geometry processing and computer graphics. He has a PhD in computer science from Koç University, Turkey. Contact him at ys@ceng.metu.edu.tr or visit http://www.ceng.metu.edu.tr/∼ys.